

Near-field radiative heat transfer between parallel structures in the deep subwavelength regime

Raphael St-Gelais^{1,2}, Linxiao Zhu³, Shanhui Fan³ and Michal Lipson^{1,2*}

Thermal radiation between parallel objects separated by deep subwavelength distances and subject to large thermal gradients (>100 K) can reach very high magnitudes, while being concentrated on a narrow frequency distribution. These unique characteristics could enable breakthrough technologies for thermal transport control^{1–3} and electricity generation^{4–8} (for example, by radiating heat exactly at the bandgap frequency of a photovoltaic cell). However, thermal transport in this regime has never been achieved experimentally due to the difficulty of maintaining large thermal gradients over nanometre-scale distances while avoiding other heat transfer mechanisms, namely conduction. Here, we show near-field radiative heat transfer between parallel SiC nanobeams in the deep subwavelength regime. The distance between the beams is controlled by a high-precision micro-electromechanical system (MEMS). We exploit the mechanical stability of nanobeams under high tensile stress to minimize thermal buckling effects, therefore keeping control of the nanometre-scale separation even at large thermal gradients. We achieve an enhancement of heat transfer of almost two orders of magnitude with respect to the far-field limit (corresponding to a 42 nm separation) and show that we can maintain a temperature gradient of 260 K between the cold and hot surfaces at ~100 nm distance.

Radiative heat transfer between objects separated by deep subwavelength distances can exceed the conventional laws of thermal radiation^{9,10}, while being concentrated over a quasi-monochromatic frequency range¹¹. This heat transfer occurs through evanescent coupling of thermally excited surface resonances and consequently scales inversely with separation (as $1/d^\alpha$, where α is a geometry-dependent factor). The separation d at which this regime occurs depends on the geometry of the system and on the materials involved, but is generally around 200 nm for identical parallel structures relying on surface phonon resonances¹². For applications such as electricity generation and thermal control, the two materials involved are non-identical, such that resonant coupling is less efficient and separations <100 nm are typically required^{6,13}.

The unique features of heat transfer in the deep subwavelength regime (that is, large magnitude and quasi-monochromatic spectral distribution) could allow high-efficiency generation of electricity from heat^{4,6–8} and novel thermal control devices^{1,3}. For example, near-field heat transfer between a hot thermal emitter and a cold photovoltaic cell could allow energy conversion with a greater efficiency (>30% for a $T = 600$ K heat source⁸) than when using either a thermoelectric generator or single-junction solar photovoltaic cells. It is also predicted that engineering the surface resonance frequencies of parallel structures could allow novel thermal control devices such as thermal rectifiers^{1,2} or thermal transistors³.

These applications rely on radiative heat transfer between parallel structures in the deep subwavelength regime and on a high temperature gradient between them, neither of which have been achieved

experimentally. Near-field enhancement of heat transfer has been demonstrated between parallel plates using active parallelism control^{14–16} or mechanical spacers^{4,17,18}. The smallest separation achieved in these experiments was 500 nm (ref. 18; with a 20 K thermal gradient), which is small enough to overcome the far-field blackbody radiation limit, but not enough to reach the deep subwavelength regime where the heat flux is effectively concentrated around a single frequency¹². Furthermore, the highest temperature gradient (ΔT) achieved in these experiments was 85 K¹⁷ (for a 1.6 μm separation), which is relatively small, especially for energy conversion applications where the generated power and the efficiency η both scale with the temperature gradient (for example, $\eta_{\text{Carnot}} = \Delta T/T_{\text{hot}}$). In sphere-plane geometries^{19–21}, distances as low as 20 nm²¹ were achieved, which is close to the distance where the deep subwavelength regime occurs (typically 10–20 nm)²⁰. In this configuration, however, the effective heat transfer area is small and hence not practical for energy conversion applications where the power is proportional to the area. From the proximity approximation, the sphere in such geometry can be considered as a geometrical distribution of planar surfaces²⁰. Given that the heat transfer between parallel planes decays with distance as $1/d^2$, the effective heat transfer decays quickly away from the tip of the sphere. This limitation does not occur in a parallel geometry, where all regions of the surfaces involved contribute equally to the heat transfer.

We used parallel nanobeams monolithically integrated with electrostatic comb drive actuators (Fig. 1) to achieve heat transfer between two parallel nanobeams in the deep subwavelength regime. These actuators allow precise displacement control, limited in theory to subnanometre precision by Brownian motion and by actuation voltage uncertainty (Supplementary Section 1). Their power consumption (<200 pW in the on state due to ~1–2 pA leakage current through the capacitor at 150 V actuation voltage) is at least three orders of magnitude lower than the power applied to the heated beam (ranging from 1.4 to 66 μW , depending on the targeted temperature) and consequently has a negligible influence on the temperature of the system.

We relied on the surface phonon–polariton resonance of SiC to create the surface waves responsible for near-field heat transfer. Note that, although there has been a lot of theoretical work on near-field heat transfer with thin SiC films^{1,5,22–24}, no experimental work has been reported. We used SiC deposited by plasma-enhanced chemical vapour deposition (PECVD) and annealed to create a microcrystalline (μ -SiC) phase (see Methods). We characterized the infrared permittivity ϵ of μ -SiC and found it to be well described by a Lorentz–Drude relation (equation (1)) that has a sharper infrared resonance than most commonly used SiO₂:

$$\epsilon(\omega) = \epsilon_\infty \left(1 + \frac{\omega_L^2 - \omega_T^2}{\omega_T^2 - \omega^2 - i\Gamma\omega} \right) \quad (1)$$

¹School of Electrical and Computer Engineering, Cornell University, Ithaca, New York 14853, USA. ²Department of Electrical Engineering, Columbia University, New York, New York 10027, USA. ³Ginzton Laboratory, Stanford University, Stanford, California 94305, USA. *e-mail: ml3745@columbia.edu

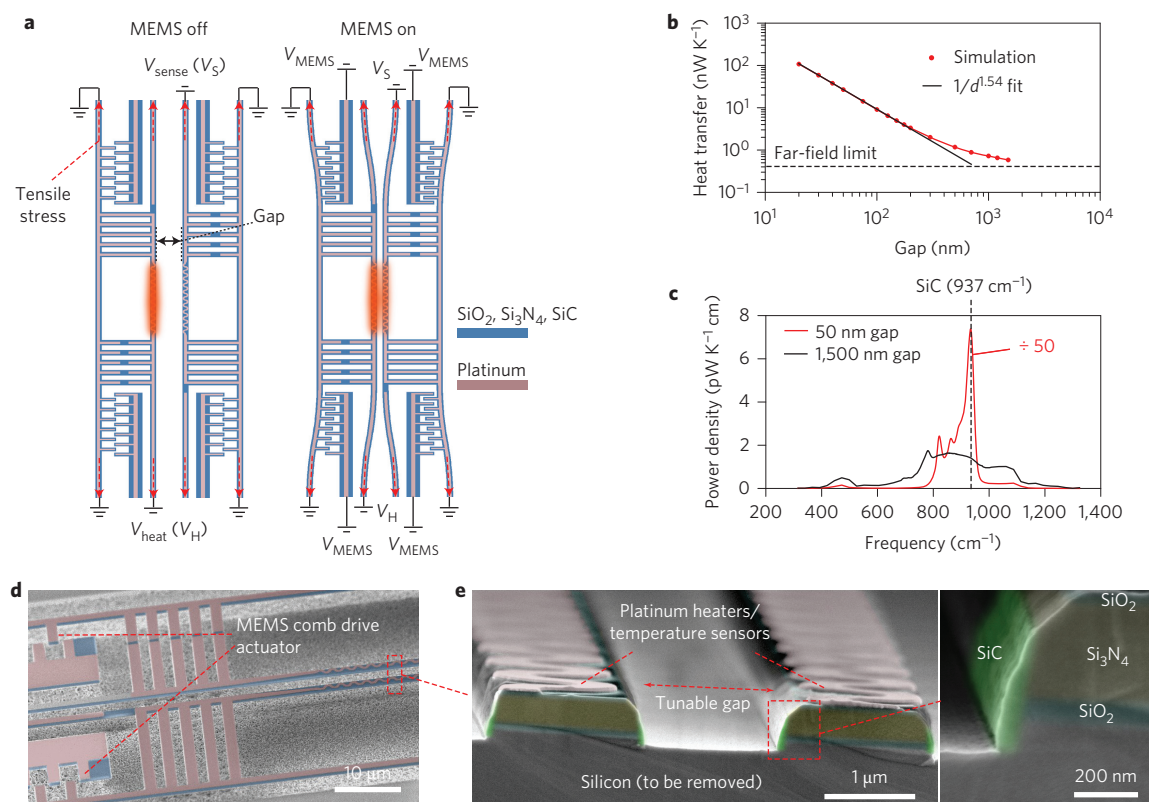


Figure 1 | Device overview and operating principle. MEMS with integrated electrical heaters/temperature sensors are used to bring together two parallel nanobeams and reach the deep subwavelength heat transfer regime. **a**, Schematic of the MEMS geometry (not to scale) and operation principle. Applying a voltage (V_{MEMS}) on the interdigitated comb drive closes the gap between the nanobeams, from 1,500 nm initially (left) to sub-100 nm (right). A V_{heat} voltage is applied to heat one of the beams, while the V_{sense} voltage on the other beam allows for temperature sensing. High tensile stress allows for mechanical stability at high temperatures. **b**, Simulated radiative heat transfer between two nanobeams as a function of distance between them. The hot beam is set at $T = 10 \text{ K}$ above room temperature (293 K). The deep subwavelength regime occurs for beam separation below 200 nm, where the heat transfer begins to scale as $1/d^{1.54}$ (which appears linear on a logarithmic scale). **c**, Simulated heat transfer spectrum between the nanobeams at two different separations. For $d = 50 \text{ nm}$, the heat transfer is concentrated mainly around the SiC surface resonance (near $\omega = 937 \text{ cm}^{-1}$). The secondary peaks at lower frequencies are caused by the presence of Si_3N_4 and SiO_2 . **d**, False-colour scanning electron micrograph (SEM) of the device after structural release. **e**, SEM false-colour cross-section view of the nanobeams before structural release.

where $\omega_T = 789 \text{ cm}^{-1}$ and $\omega_L = 956 \text{ cm}^{-1}$ are respectively the transverse and longitudinal optical phonon frequencies, $\epsilon_\infty = 8$ and $\Gamma = 20 \text{ cm}^{-1}$ (Supplementary Fig. 1, for characterization and extended discussion see Supplementary Section 2). Such sharper resonance does not necessarily result in a stronger enhancement (calculations²⁵ show that SiO_2 and SiC yield similar enhancements), but could be beneficial to heat flow control applications that rely on the quasi-monochromatic nature of near-field heat transfer¹.

We simulated the heat transfer between the nanobeams using a Fourier modal method based on the fluctuational electrodynamics formalism^{26,27} (see Methods) and we predicted that the deep subwavelength regime occurs at distances $< 200 \text{ nm}$. The dimensions and geometrical arrangement considered for these simulations are presented in Supplementary Figs 2 to 4. For distances smaller than 200 nm (Fig. 1b) the simulated results follow the typical $1/d^\alpha$ law that is characteristic of the deep subwavelength regime, with $\alpha = 1.54$. The simulations also show that heat transfer in the deep subwavelength regime is quasi-monochromatic (Fig. 1c) and centred around the $\epsilon(\omega) = -1$ surface phonon resonance frequency of SiC (937 cm^{-1}). The small secondary peaks at lower frequency in Fig. 1c are caused by the finite dimensions of the beams and by the presence of materials other than SiC (that is, Si_3N_4 and SiO_2), which are accounted for in the simulation (see Methods). Although it would be very challenging to analytically simulate heat transfer for such a complex geometry and compare our numerical

simulations, we note that the $\alpha = 1.54$ geometry factor is consistent with what can be calculated using the proximity approximation between two cylinders ($\alpha = 1.5$). The fact that α is slightly larger in our numerical simulation might indicate that our geometry is intermediate between a two-cylinder case ($\alpha = 1.5$) and the two-dimensional parallel-plane case ($\alpha = 2$).

To achieve, experimentally, very small distances over large areas, it is critical that the two surfaces are completely parallel. Therefore, no buckling should occur under changes of temperature. We prevented buckling by designing the beams such that they preserved the high tensile stress of silicon nitride ($\sim 900 \text{ MPa}$) after structural release (Fig. 1a). This stress prevented the thermal bimorph effect from causing the buckling that would catastrophically impact the minimum achievable distance in our system at high temperatures (Fig. 2). Our design also suppresses the stress-induced deformation that prevented us from reaching the deep subwavelength regime with our previous platform²⁸.

To measure the heat transfer, the beams were brought together by sweeping the voltage supplied to the MEMS actuator (V_{MEMS} in Fig. 1a) while the temperatures of the heated beam (T_{heat}) and the sensing beam (T_{sense}) were measured (see Methods). The result of this scan is presented in Fig. 3b, where the inset shows the transition between near-field and contact regimes. The displacement of the nanobeams as a function of the MEMS voltage was also measured in a separate experiment (Supplementary Section 1)

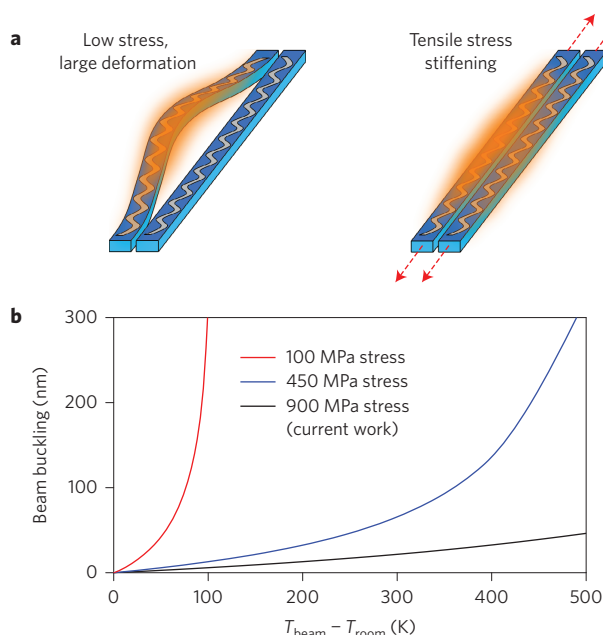


Figure 2 | Exploiting tensile stress to avoid thermomechanical

deformations. Tensile stress in the nanobeams minimizes thermal buckling that would be detrimental to the minimum achievable separation at high temperatures. **a**, Schematic of nanobeam buckling due to the thermal bimorph effect. **b**, Simulated buckling of a doubly clamped, 600- μm -long, bimaterial beam made of Si_3N_4 (300 nm thick) and Pt (50 nm thick).

and is presented in Fig. 3a. The experimental data of Fig. 3 were converted to normalized heat transfer power (q , in W K^{-1}) using

$$q = \frac{XP_{\text{heat}}T_{\text{sens}}}{(T_{\text{heat}} - T_{\text{sens}})(T_{\text{heat}} + XT_{\text{sens}})} \quad (2)$$

where ($X = \sigma_{\text{sens}}/\sigma_{\text{heat}}$) is the ratio of the background heat conduction σ of the two nanobeams, and P_{heat} is the supplied heating power. The derivation of equation (2) from the thermal equivalent circuit of the experiment (Supplementary Fig. 5) is presented in Supplementary Section 4. From the symmetry of the system, $X \approx 1$ for scans of relatively low temperature amplitude such as in Fig. 3b.

The measured heat transfer agrees well with the simulated values. Figure 4a plots the experimental heat transfer power and compares it with the simulated data (which is fitted vertically and horizontally, see Methods). At gaps larger than ~ 150 nm, the experimental values are slightly larger than the simulated ones. This could be caused by a larger infrared material absorption coefficient (of, for example, Si_3N_4) than considered in the simulations, which would increase the contribution of the propagating wave to the heat transfer. This increase causes the deep subwavelength regime to occur at <150 nm distances, rather than <200 nm in the simulated data (Fig. 1b). At gaps smaller than 150 nm, the experimental data match the simulation more closely, and small deviations between simulation and experiments are visible only in the logarithmic-scale inset in Fig. 4a. These are probably caused by the inability of the polynomial fit to perfectly match the experimental MEMS displacement in Fig. 3a, or by slightly different experimental conditions between the MEMS displacement measurement (Supplementary Section 1) and the heat transfer measurement.

We achieved an 82 times enhancement of heat transfer (34 nW K^{-1} , Fig. 4a) over the far-field limit (0.42 nW K^{-1}) and were able to maintain the nanobeams in the deep subwavelength regime for

temperature gradients as high as 260 K. We define the far-field limit as the maximum power that the SiC surface of the nanobeam can radiate to the far-field, at a given temperature (see Methods). This enhancement corresponds to a 42 nm gap between the nanobeams, which is well within the deep subwavelength regime (<150 nm). The measurement of Fig. 4a was repeated for different temperatures of the heated beam. In Fig. 4b, the minimum achieved gap (that is, the smallest near-field gap achieved before the beams came into contact with each other) is reported as a function of the heated beam temperature. The minimum achieved near-field gap increases slightly with temperature. This is most probably due to the thermal buckling that occurs despite the large stiffness of the nanobeams. The increase is indeed consistent with the simulated buckling presented in Fig. 2. We reached the deep subwavelength regime (that is, distance <150 nm) for heated beam temperatures as high as 720 K (that is, 425 K above room temperature). In this case, the sensing beam temperature reached 460 K, such that the net temperature gradient between the beams was 260 K (Supplementary Fig. 6). Such high thermal gradient translates to a net energy flux of $>6 \text{ W cm}^{-2}$ (Fig. 4c).

We have demonstrated near-field radiative heat transfer between parallel beams in the deep subwavelength regime under a high temperature gradient. We envision that this

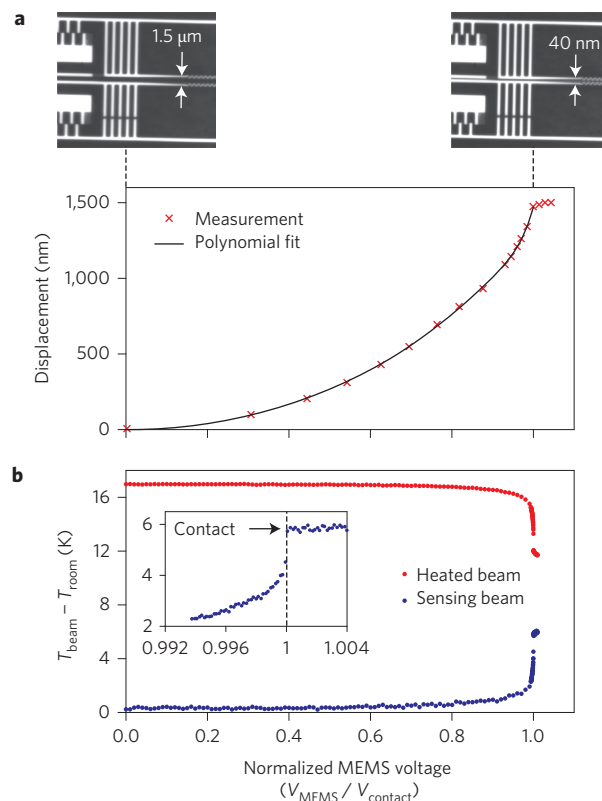


Figure 3 | Measurement of temperature changes as a function of

nanobeam separation. Increasing the voltage applied to the MEMS actuators closes the gap between the two nanobeams and leads to radiative heat exchange. **a**, Measured and fitted displacement of the nanobeams as a function of the voltage on the MEMS actuator. Optical micrographs, such as those presented above the graph for the largest (left) and smallest (right) gaps, are processed by an image treatment algorithm to extract the displacement. **b**, The temperature of the heated beam (T_{heat}) and the sensing beam (T_{sens}) as a function of the voltage on the MEMS actuator shows that strong heat exchange occurs as the beams are brought closer. The inset (magnification of the same data) shows a clear transition at the point the beams make contact.

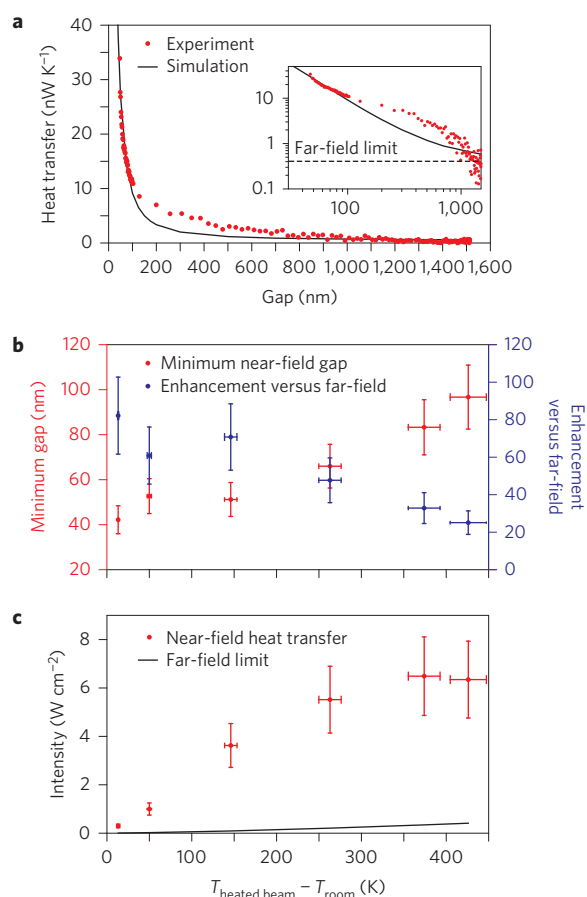


Figure 4 | Heat transfer in the deep subwavelength regime over a wide range of temperatures. Heat transfer measurements are compared with Fourier modal method simulations, showing that we reach the deep subwavelength regime for a wide range of heated beam temperatures.

a, Measurement and simulation (fitted, see Methods) of heat transfer between the nanobeams as a function of separation. Inset: the same data, on a logarithmic scale. The measured heat transfer at the smallest gap is 82 times higher than the far-field limit, which corresponds to a 42 nm gap between the beams. In this case, the heated beam temperature (relative to $T_{\text{room}} = 293$ K) is 13 K (Fig. 3b). **b**, Minimum gap (that is, before the beams make contact) and maximum enhancement (relative to the far-field limit) achieved for various heated beam temperatures. Heat transfer remains in the deep subwavelength regime (gap < 150 nm) for heated beam temperatures as high as 720 K. In this case, the sensing beam temperature is 460 K, such that the net temperature gradient is 260 K. **c**, Near-field heat transfer intensity (power per unit area) as a function of the temperature of the heated beam (the area is taken as the inner SiC surface of the nanobeams). Errors bars in **b** and **c** are calculated from uncertainty regarding the thermal coefficient of resistance and the effective beam interaction length (Supplementary Fig. 3).

nanoscale approach can be conducive to applications of near-field heat transfer, especially in near-field thermophotovoltaic energy conversion. Our approach produces a high net energy flux between the beams (Fig. 4c), which, for energy conversion applications, is often more crucial than relative enhancement over far-field radiation. We also note that our approach could be scaled up to a larger effective area by simply arraying several nanobeams (on top of a photovoltaic cell, for example) and by individually controlling their out-of-plane displacement using MEMS actuators. Our work shows that the power consumption of such actuators (<200 pW in the present case) can be orders of magnitude lower than the radiated power (up to 6.6 μ W, at

$T_{\text{heated beam}} - T_{\text{room}} = 425$ K, Fig. 4c) and could hence be negligible compared to the generated electrical power.

Methods

Methods and any associated references are available in the [online version of the paper](#).

Received 9 October 2015; accepted 26 January 2016; published online 7 March 2016

References

- Otey, C. R., Lau, W. T. & Fan, S. Thermal rectification through vacuum. *Phys. Rev. Lett.* **104**, 154301 (2010).
- Wang, L. P. & Zhang, Z. M. Thermal rectification enabled by near-field radiative heat transfer between intrinsic silicon and a dissimilar material. *Nanoscale Microsc. Therm.* **17**, 337–348 (2013).
- Ben-Abdallah, P. & Biehs, S.-A. Near-field thermal transistor. *Phys. Rev. Lett.* **112**, 044301 (2014).
- DiMatteo, R. S. *et al.* Enhanced photogeneration of carriers in a semiconductor via coupling across a nonisothermal nanoscale vacuum gap. *Appl. Phys. Lett.* **79**, 1894–1896 (2001).
- Narayanaswamy, A. & Chen, G. Surface modes for near field thermophotovoltaics. *Appl. Phys. Lett.* **82**, 3544–3546 (2003).
- Laroche, M., Carminati, R. & Greffet, J.-J. Near-field thermophotovoltaic energy conversion. *J. Appl. Phys.* **100**, 063704 (2006).
- Park, K., Basu, S., King, W. P. & Zhang, Z. M. Performance analysis of near-field thermophotovoltaic devices considering absorption distribution. *J. Quant. Spectrosc. Radiat. Transfer* **109**, 305–316 (2008).
- Ilic, O., Jablan, M., Joannopoulos, J. D., Celanovic, I. & Soljacic, M. Overcoming the black body limit in plasmonic and graphene near-field thermophotovoltaic systems. *Opt. Express* **20**, A366–A384 (2012).
- Cravalho, E. G., Tien, C. L. & Caren, R. P. Effect of small spacings on radiative transfer between two dielectrics. *J. Heat Transfer* **89**, 351–358 (1967).
- Polder, D. & Van Hove, M. Theory of radiative heat transfer between closely spaced bodies. *Phys. Rev. B* **4**, 3303–3314 (1971).
- Shchegrov, A. V., Joulain, K., Carminati, R. & Greffet, J.-J. Near-field spectral effects due to electromagnetic surface excitations. *Phys. Rev. Lett.* **85**, 1548–1551 (2000).
- Mulet, J.-P., Joulain, K., Carminati, R. & Greffet, J.-J. Enhance radiative heat transfer at nanometric distances. *Microscale Thermophys. Eng.* **6**, 209–222 (2002).
- Iizuka, H. & Fan, S. Rectification of evanescent heat transfer between dielectric-coated and uncoated silicon carbide plates. *J. Appl. Phys.* **112**, 024304 (2012).
- Ottens, R. S. *et al.* Near-field radiative heat transfer between macroscopic planar surfaces. *Phys. Rev. Lett.* **107**, 014301 (2011).
- Kralik, T. *et al.* Strong near-field enhancement of radiative heat transfer between metallic surfaces. *Phys. Rev. Lett.* **109**, 224302 (2012).
- Ijro, T. & Yamada, N. Near-field radiative heat transfer between two parallel SiO₂ plates with and without microcavities. *Appl. Phys. Lett.* **106**, 023103 (2015).
- Hu, L., Narayanaswamy, A., Chen, X. & Chen, G. Near-field thermal radiation between two closely spaced glass plates exceeding Planck's blackbody radiation law. *Appl. Phys. Lett.* **92**, 133106 (2008).
- Ito, K., Miura, A., Iizuka, H. & Toshiyoshi, H. Parallel-plate submicron gap formed by micromachined low-density pillars for near-field radiative heat transfer. *Appl. Phys. Lett.* **106**, 083504 (2015).
- Shen, S., Narayanaswamy, A. & Chen, G. Surface phonon polaritons mediated energy transfer between nanoscale gaps. *Nano Lett.* **9**, 2909–2913 (2009).
- Rousseau, E. *et al.* Radiative heat transfer at the nanoscale. *Nature Photon.* **3**, 514–517 (2009).
- Song, B. *et al.* Enhancement of near-field radiative heat transfer using polar dielectric thin films. *Nature Nanotech.* **10**, 253–258 (2015).
- Francœur, M., Mengüç, M. P. & Vaillon, R. Near-field radiative heat transfer enhancement via surface phonon polaritons coupling in thin films. *Appl. Phys. Lett.* **93**, 043109 (2008).
- Miller, O. D., Johnson, S. G. & Rodriguez, A. W. Effectiveness of thin films in lieu of hyperbolic metamaterials in the near field. *Phys. Rev. Lett.* **112**, 157402 (2014).
- Basu, S., Yang, Y. & Wang, L. Near-field radiative heat transfer between metamaterials coated with silicon carbide thin films. *Appl. Phys. Lett.* **106**, 033106 (2015).
- Joulain, K., Mulet, J.-P., Marquier, F., Carminati, R. & Greffet, J.-J. Surface electromagnetic waves thermally excited: radiative heat transfer, coherence properties and Casimir forces revisited in the near field. *Surf. Sci. Rep.* **57**, 59–112 (2005).
- Lussange, J. *et al.* Radiative heat transfer between two dielectric nanogratings in the scattering approach. *Phys. Rev. B* **86**, 085432 (2012).
- Otey, C. R., Zhu, L., Sandhu, S. & Fan, S. Fluctuational electrodynamics calculations of near-field heat transfer in non-planar geometries: a brief overview. *J. Quant. Spectrosc. Radiat. Transfer* **132**, 3–11 (2014).

28. St-Gelais, R., Guha, B., Zhu, L., Fan, S. & Lipson, M. Demonstration of strong near-field radiative heat transfer between integrated nanostructures. *Nano Lett.* **14**, 6971–6975 (2014).

Acknowledgements

The authors acknowledge support from the Defense Advanced Research Projects Agency for award FA8650-14-1-7406, supervised by Avram Bar-Cohen. This work made use of the Cornell Center for Materials Research Shared Facilities, which are supported through the National Science Foundation (NSF) Materials Research Science and Engineering Centers programme (DMR-1120296), and the Cornell NanoScale Facility, a member of the National Nanotechnology Infrastructure Network, which is supported by the NSF (grant ECCS-0335765). R.S.G. held subsequent postdoctoral fellowships from the Fonds de recherche du Québec–Nature et Technologies (FRQNT) and from the Natural Sciences and Engineering Research Council of Canada (NSERC) during this work.

Author contributions

All authors participated in conceiving the experiment, discussed the results and commented on the manuscript. R.S.G. conceived of the MEMS platform, performed the μ -SiC material characterization, fabricated the device, performed the experimental measurements and drafted the manuscript. L.Z. performed the Fourier modal method heat transfer simulations. R.S.G. and L.Z. interpreted the experimental data.

Additional information

Supplementary information is available in the [online version of the paper](#). Reprints and permissions information is available online at www.nature.com/reprints. Correspondence and requests for materials should be addressed to M.L.

Competing financial interests

The authors declare no competing financial interests.

Methods

Microcrystalline silicon carbide (μ -SiC) deposition. Amorphous silicon carbide was first deposited by plasma-enhanced chemical vapour deposition (PECVD) from silane (SiH_4) and methane (CH_4) gas precursors in a 1:20 ratio and with argon as a dilution gas. The film was then annealed in an argon atmosphere at 1,100 °C for 90 min to grow a microcrystalline phase²⁹. The silane/methane concentration ratio was optimized by measuring the refractive index of the film by ellipsometry after the anneal process. The 1:20 ratio yielded a 2.53 refractive index (at $\lambda = 1,500$ nm), which is very close to the theoretical value (2.57). Higher or lower ratios both led to higher refractive indices, which is consistent with the growth of silicon or carbon clusters during annealing of non-stoichiometric films.

Device fabrication. A $\text{SiO}_2/\text{Si}_3\text{N}_4/\text{SiO}_2$ film stack was first deposited on a conventional silicon wafer by low-pressure chemical vapour deposition (LPCVD). The structure was then defined by deep-ultraviolet lithography and anisotropically etched with fluorine chemistry. SiC was then deposited over the structure by PECVD and annealed at 1,100 °C to grow the μ -SiC phase. SiC was anisotropically etched with fluorine chemistry, such that the μ -SiC remained only on the nanobeam sidewalls. Platinum heaters and metal contact were deposited by electron-beam evaporation and liftoff using a chrome adhesion layer. The device was finally released by undercutting the silicon substrate with XeF_2 chemistry.

Numerical simulation method. We simulated the radiative heat transfer between the beams using fluctuational electrodynamics based on a Fourier modal method, for the geometry shown in Supplementary Fig. 2. Using the SEM image in this figure, we approximated the SiC surface by five blocks of different thicknesses (from 18 to 76 nm), to take into account the slightly non-vertical beam profile. The Si_3N_4 and SiO_2 layers were also included in the simulation and were each approximated as single blocks. In these calculations, the beams were treated as infinitely long, as their length is large (200 μm) compared to all beam cross-section dimensions (<2 μm). For the Fourier modal method calculations, the two beams were periodically repeated in space (Supplementary Fig. 4) to allow for Fourier expansion. The period was set to be large, such that the heat transfer between the facing beams dominated the heat transfer (that is, the heat transfer between each period was negligible). The thermal excitations, permittivity profile and fields in each patterned layer were all expanded in Fourier space. We used a scattering matrix formalism to relate the Fourier modal amplitudes between the layers.

Experimental condition and procedure. The heat transfer experiments were performed at room temperature in a high-vacuum (9×10^{-5} torr) electrical probe station. Electrical measurements were performed using an Agilent B1500 semiconductor parameter analyser. The MEMS voltage (V_{MEMS}) was swept to bring the two nanobeams together while constant heating (V_{heat}) and sensing (V_{sens}) voltages were supplied to each of the two nanobeams. The time interval between each MEMS voltage increment (50 ms) was several times larger than the thermal response time of the system (7 ms), such that all measurements were in a steady state.

V_{sens} was kept much lower than V_{heat} , such that the power supplied to the sensing beam was always at least 25 times lower than the power supplied to the heated beam (P_{heat}). These constant voltages were also used to measure the temperature of the two beams, through the variation of their electrical resistance R as $\Delta R/R = \text{TCR} \times \Delta T$, where $\text{TCR} = 0.00166 \text{ K}^{-1}$ is the measured temperature coefficient of resistance of platinum (see next section).

TCR measurement. The TCR of platinum was measured by placing the device on a hot plate ramped from room temperature to 100 °C. We observed that the TCR differed greatly after the device was used at high temperature for the first time. For this reason, before TCR measurements, a heating voltage (V_{heat}) 10% higher than the one used for the highest temperature point in Fig. 4b,c was supplied to the device under vacuum and held for 5 min until the current (and hence the electrical resistance) stabilized. After this procedure, the device was placed on a hot plate ramped from room temperature to 100 °C and the resistance was measured at every 3 °C increment. We found that the thermal coefficient of resistance was 0.00125 K^{-1} before the annealing procedure and $\text{TCR} = 0.00166 \text{ K}^{-1}$ after. We estimated a $\pm 5\%$ error on this value from the repeatability of the measurement.

Fitting procedure. In Fig. 3a, the measured displacement as a function of the MEMS voltage was fitted using an eighth-order polynomial. The fitted function was subsequently used to convert the MEMS voltage to displacement values. The polynomial order was chosen iteratively to be high enough to match the experimental points well, while being low enough to minimize spurious oscillation between the experimental points.

For Fig. 4a, the experimental and theoretical data were fitted together in two different ways. First, the experimental data were translated horizontally to account for the uncertainty regarding the initial gap between the nanobeams (that is, the relative displacement of the beam is well known from Fig. 3a, but the exact initial separation is unknown). The initial gap that best fit the experimental results was 1,514 nm, close to the designed 1,500 nm value. Second, the experimental data were translated vertically to account for parasitic heat conduction through the substrate. The translation that best fit the experiment is 1 nW K^{-1} , which is negligible compared to the achieved radiative heat achieved at the smallest gap (34 nW K^{-1}).

Far-field limit calculation. We define the far-field limit as the maximum power that can be radiated to the far-field by the inner silicon carbide part of the heated nanobeam. This calculation was performed using the Fourier modal method^{26,27}. The far-field temperature in this simulation was set to room temperature (293 K).

Reference

- Calcagno, L., Musumeci, P., Roccaforte, F., Bongiorno, C. & Foti, G. Crystallization process of amorphous silicon-carbon alloys. *Thin Solid Films* **411**, 298–302 (2002).